FULL PAPER

Gilding

ADVANCED
FUNCTIONAL
MATERIALS

www.afm-journal.de

Gilding with Graphene: Rapid Chemical Vapor Deposition Synthesis of Graphene on Thin Metal Leaves

Kaihao Zhang, Charalampos Androulidakis, Mingze Chen, and Sameh Tawfick*

Gilding is the ancient process of coating intricate artifacts with precious metals. Fascinating Egyptian and Chinese sculptures, coated with <200 nm thin metal films by this process, have resisted corrosion, wear, and other environmental degradations for thousands of years. Here, 150 nm thin palladium leaves are enriched by doped with a single layer of graphene. Commercially available Pd leaves are uniquely suited for graphene synthesis by a highly dynamic chemical vapor deposition process. The Pd leaves made by high strain rate beating are stable at high synthesis temperature, resisting solid-state dewetting owing to their extremely low grain triple junctions density (0.017 μm^{-1}). Mathematical models of growth kinetics guide the development of extremely rapid synthesis conditions, resulting in the formation of high-quality graphene on Pd in less than a minute, owing to the graphene grains growing twice as fast as copper-catalyzed growth. The graphene monolayer on the leaf increases the effective surface modulus by 59% to 236 GPa. Uniaxial strain testing with Raman spectroscopy reveals the excellent crystallinity of graphene by probing the stress-induced phonon shifts. This new material could open exciting opportunities in utilizing high-quality 2D materials to coat large structures.

1. Fabrication of Pd-Gr leaf for Nanogilding

With the development of metallurgy in 2nd millennium B.C., the beating of pure metal into ultrathin leaves, less than 200 nm thick, was developed and extensively used for "gilding" temple walls, precious furniture, and sculptures.[1] Leaves of gold, silver, and copper having high purity were carefully laminated over the base stones, metals, and wood, for example, Tutankhamun's middle coffin[2,3] as shown in **Figure 1**a. This coating process is ubiquitously seen in artifacts having various sizes and materials.[4–6] This ancient decoration technique not only enriches the artwork with tiny amounts of precious metals, but also protects these precious artifacts owing to outstanding corrosion and wear resistance of these metals.[4] Today, gilding is still used as a contemporary art for coating small scale artifacts as well as skyscrapers as seen in the gold leaf-gilded roof of Carbide & Carbon Building[7] in Chicago, illustrated in

K. Zhang, Dr. C. Androulidakis, M. Chen, Dr. S. Tawfick
Mechanical Science and Engineering
University of Illinois Urbana-Champaign
Urbana, IL 61801, USA
E-mail: tawfick@illinois.edu

The ORCID identification number(s) for the author(s) of this article can be found under https://doi.org/10.1002/adfm.201804068.

Figure 1b. The ultrathinness of the metal leaves is crucial for the smooth conformation onto relatively rough surfaces. Drops of liquids or adhesives are applied on the surface before the leaves are laminated to tighten the gap between the leaves and the surface of the coated surface by capillary forces. To achieve the required thinness, the leaves are worked by repeated beating of thick metal foils. Ancient cultures used stones to manually beat a stack of sub-millimeter thick metal foils supported on a flat anvil until their thickness reaches 100–200 nm, while their area increases by several million folds.[6] Today, hydraulic hammers are used to strike a stack of metal foil several thousand times at high strain rate. The extreme thinning is enabled by passively controlling the thermomechanics of metalworking. During beating, the metal layers are sandwiched between low surface energy sheets derived from plant fibers to allow well-lubricated flow of the metal, and facilitate the isolation and manipulation of individual freestanding <200 nm thin leaves, which can then be used for gilding. The thin leaves have typical dimensions of 5 × 5 in^2 with 100–200 nm thickness, yet their unique microstructure enables their manual manipulation as freestanding foils despite their extreme thinness. To our knowledge, the details of the metal microstructure as well as the thermomechanical transformations in this ancient process have not been studied using modern characterization techniques. The production of 100 nm thin leaves is indeed a fascinating 4000-year-old nanomanufacturing process.

The objective of this study is to use thin metal leaves as substrates for high-quality monolayer graphene synthesis, and demonstrate the applicability of the palladium-graphene (Pd-Gr) composite leaves in gilding. Metal leaves offer many advantages as a scalable coating materials owing to their commercial availability in large rolls and low price compared to thin film deposition by vacuum thin film deposition such as sputtering or e-beam evaporation. Moreover, since they are used to gild and coat large structures, enriching them with a monolayer of graphene will not significantly affect their optical properties but offers attractive enhancements in their surface modulus, and potentially their hardness, friction, wear, scratch resistance, etc., as well as additional chemical functionalization. In this study, we demonstrate the use of commercially available Pd leaves, successfully coated with a monolayer graphene by chemical vapor deposition (CVD), to gild a 3D printed sculpture,

**ADVANCED
SCIENCE NEWS**

www.advancedsciencenews.com

**ADVANCED
FUNCTIONAL
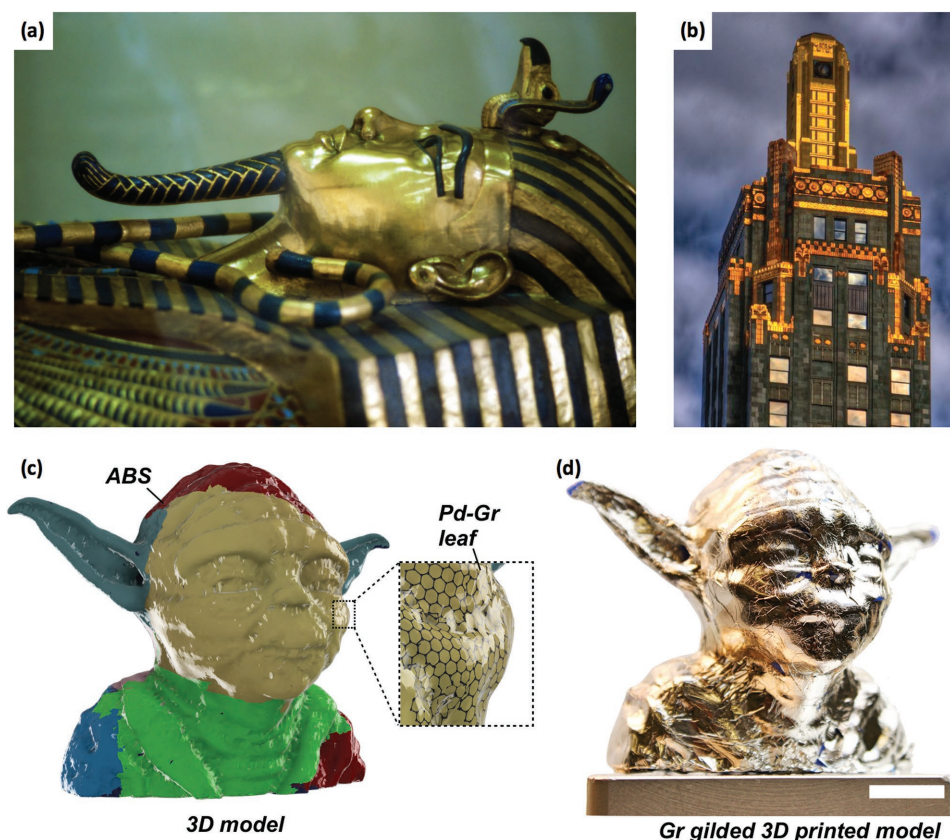MATERIALS**

www.afm-journal.de

Figure 1. Gilding with ultrathin metal leaves. a) Photograph of the gold leaf-gilded wooden coffin of Tutankhamun. Reproduced with permission.[3] Copyright: Griffith Institute, University of Oxford. b) Photograph of Carbide & Carbon Building in Chicago. Reproduced with permission.[7] Copyright 2010, Thaddeus Roan. c) A CAD model for 3D printing. The colored regions illustrate the placement of individual leaves for gilding with Pd-Gr. The CAD model used for printing was kindly provided by Barak Moshe at https://www.thingiverse.com/thing:10650. d) Photograph of Pd-Gr leaf-gilded 3D printed model. Scale bar: 1 cm.

illustrated in Figure 1c,d, to demonstrate the viability of the graphene enrichment without compromising the characteristic of the leaves which lend them suitable for surface coating.

Graphene, a 2D lattice of sp^2-hybridized carbon atoms, is very attractive due to its superb in-plane mechanical strength, low friction, wear and corrosion resistance.[8] One promising route to harness these properties for applications is to incorporate graphene on the surface or the bulk of metal structures, for example, to create composite materials.[9,10] It is possible to synthesize large-area graphene sheets on thick metal foils via CVD.[11–14] Several metals can be used as catalyst material. They can be grouped into two broad types: Group 1: metals having low carbon solubility and low graphene binding energy (the copper and platinum group); and Group 2: metals having high carbon solubility and strong graphene binding energy (the nickel and palladium group). Metal catalysts from Group 1 offer self-limited monolayer graphene synthesis by surface adsorption and hence are suitable for obtaining graphene for electronic devices. The synthesis on Cu and Pt proceeds by slow isothermal adsorption at high temperature, and the metal catalyst is typically chemically etched to release the graphene monolayer and transfer it to device substrates. In this study, we focus on graphene synthesis on Pd leaves, which belongs to Group 2, for several reasons: (1) our intention is to dope the metal with graphene for gilding and hence strong binding

between the monolayer graphene and the metal catalyst is required; (2) the leaves are extremely thin, and hence we need a highly active catalyst for extremely rapid synthesis before the leaf becomes unstable by solid-state dewetting. Pd exhibits high binding energy and low separation distance to the graphene of 84 meV atom^{-1} and ≈ 2.5 Å respectively,[15,16] which makes it a promising candidate for gilding applications.

Commercially available Pd leaves having ≈150 nm in thickness are promising substrates for the synthesis of high-quality monolayer graphene by low pressure CVD (LPCVD) at temperatures exceeding 1000 °C. To develop the required graphene synthesis recipes for thin film catalysts, it is necessary to first consider the effect of the high synthesis temperatures on the microstructure stability. Specifically, it is challenging to grow uniform and high-quality monolayer graphene on nanoscale thin metal films via CVD. Thin metal films are unstable at high temperatures.[17] Metals tend to minimize their free surface energy by solid-state dewetting. Dewetting is driven by several processes including grooving at the grain boundaries and triple junctions, hole formation, edge retraction, and fingering instability. Nanometer thin film breaks into discrete islands at temperatures as low as one half of the melting temperature of the corresponding bulk metal, and challenges graphene synthesis since most CVD processes require long duration at temperatures significantly higher than the onset of dewetting.[17]

Moreover, synthesis of graphene on sub-micrometer thin catalysts is also challenged by the carbon atoms diffusion kinetics because it takes much shorter duration to saturate thin film catalysts compared to thick foils having >10 µm thickness. The extreme thinness limits the flux of carbon from the gas into the bulk of the catalyst typically leading to multilayered graphene growth. This leaves only a narrow window of suitable conditions for the segregation of precisely a single layer of graphene on catalysts such as Pd having high carbon solubility.[18,19]

In this study, we use Pd leaves, which offer high resistance to dewetting and high catalytic activity, combined with developing ultrafast growth recipes to overcome the challenges of graphene synthesis on ultrathin metal films. These recipes are guided by mathematical kinetics model of carbon diffusion and segregation during the CVD process. We study the Pd-Gr interface using in situ Raman spectroscopy during uniaxial stretching test of the leaves after synthesis. We use atomic force microscopy (AFM) nanoindentation to measure the enhancement of the leaves' surface stiffness owing to the graphene monolayer. This study shows the viability of producing graphene enriched leaves for coating of large structures.

Figure 2 illustrates the fabrication processes of Pd-Gr composite leaves. Commercially available Pd leaves, shown in Figure 2a, come in a booklet of freestanding sheets separated by low surface energy paper. Scanning electron microscope (SEM) imaging (Figure 2b) shows the Pd grain structure. The average grain size is 20 µm and extends through the film thickness. Figure S1a,b (Supporting Information) shows the polycrystalline composition and the surface morphology (roughness before synthesis is ≤65.5 nm) of the Pd leaf via

X-ray diffraction (XRD) and AFM. The extremely large grain size of the commercially available thin Pd leaves makes them more suitable for synthesis compared to thin film made by e-beam evaporation or sputtering.[14,20] A freestanding Pd leaf is typically laminated on a SiO$_2$/Si substrate and annealed at 500 °C for 5 h, as sketched in Figure 2c (see the Supporting Information for catalyst preparation). The annealing step releases the residual strains associated with the lamination of the Pd leaf on the substrate. After annealing, the substrate supporting the Pd leaf is removed from the furnace using a transfer arm. The furnace temperature is then increased to the synthesis temperature of 1100 °C. When furnace temperature T_f stabilizes at 1100 °C, CH$_4$ (50 sccm) is introduced 10 min before the Pd is inserted in the hot zone for a short duration (see Figure S2, Supporting Information). During the growth, the vacuum is maintained at 1.72 Torr. The substrate is then rapidly retracted out of the hot zone at a velocity of 0.5 m s^{-1} while maintaining a controlled flow of CH$_4$ and He gas mixture during cooling. The crystalline graphene domains grow epitaxially over several micrometers, can traverse the metal grain boundaries, and merge with neighboring crystals to cover the whole leaf. SEM (Figure 2d) taken at the edge of the film clearly shows hexagonal-shaped graphene domains ($\theta = 120°$) on the surface of the Pd leaves, where the graphene exhibits a darker region in the SEM. The Raman spectrum of graphene on Pd is characterized by a weak signal-to-noise ratio, which is similar to the spectra of monolayer graphene on other highly binding metals such as Ni.[16] The electrochemical "bubbling" method[13] can be successfully used to transfer the graphene from the Pd leaf
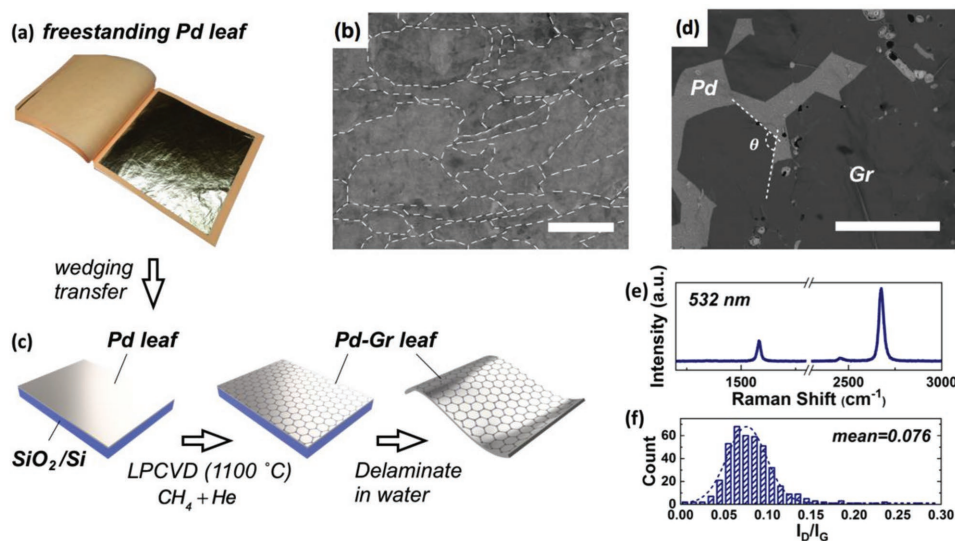

Figure 2. Fabrication of Pd-graphene (Pd-Gr) leaves by low-pressure chemical vapor deposition (LPCVD). a) Pd leaves (140 mm × 140 mm × 150 nm) are commercially available as freestanding sheets laminated between low surface energy paper. b) Scanning electron microscope (SEM) image of the as-received Pd leaf. The dashed lines outline the grain microstructure of the leaves (average grain diameter ≈ 20 µm). Scale bar: 15 µm. c) A Pd leaf is conformally laminated on SiO$_2$/Si substrate using the capillary forces of a water film, cleaned and annealed in He at 500 °C for 5 h. Graphene is synthesized on Pd leaf by LPCVD at 1100 °C, 1.79 Torr, with CH$_4$ and He gas mixture for 30 s. After synthesis, the Pd-Gr leaf can readily delaminate from the substrate by immersing in water, leaving a freestanding sheet. d) SEM image of monolayer graphene on Pd leaf near the boundary of fully covered leaves, showing the crystalline hexagonal graphene grains. Scale bar: 50 µm. e) Raman spectrum (532 nm laser) of the as-grown graphene sheet after separation from the Pd and transfer to a SiO$_2$/Si substrate. f) Histogram of the D- to G-peaks intensity ratios obtained from Raman maps (23 µm × 23 µm) showing the low defect density of the graphene.

to SiO$_2$/Si substrate. Optical image of the transferred graphene sheet on SiO$_2$/Si is shown in Figure S3a (Supporting Information). Figure 2e shows a typical Raman spectrum for the transferred graphene sheet, with intensity ratio of 2D/G around 4.3 and 2D peak ($\approx$2676.4 cm^{-1}) that is well fitted by a single Lorentzian function with a full width at half maximum (FWHM) of $\approx$30.1 cm^{-1}. Figure 2f is the histogram of D/G ratio from a Raman map of a 23 µm × 23 µm region, comprising several graphene grains, with a mean value less than 0.08, suggesting the low defect density of the graphene monolayer, even after the severe manipulations associated with transfer (see Raman maps of a single graphene domain in Figure S3b,c, Supporting Information). After synthesis, the Pd-Gr composite leaf can be readily delaminated from the SiO$_2$/Si substrate by slowly submerging it into water, due to the wettability of the surface by the water molecules.[10,21] The Pd leaves coated with graphene monolayers can be manipulated as freestanding sheets and used in gilding as shown in Figure 1d.

2. Kinetics of Graphene Synthesis on Pd Leaf Catalyst

Pd leaves offer substantial resistance to solid-state dewetting compared to Pd films deposited by sputtering. **Figure 3**a,b shows the surface morphology of Pd leaves after heating at 1100 °C in a tube furnace for 10 and 30 s, respectively. This temperature is about 70% of the melting temperature of bulk Pd. The leaves appear completely intact after 10 s. A few small holes can be optically seen under the microscope after 30 s. After 45 s, 90% of the Pd area is still intact. In contrast, sputtered nanocrystalline Pd film (nc-Pd) severely dewets within 10 s and almost fully exposes the SiO$_2$ surface after 30 s, as shown in Figure 3c,d. Figure 3e shows the fraction of the stable Pd area (defined as retained Pd area A_{Pd} over the total area A_{tot}) of Pd leaf and sputtered Pd film when heated at 1100 °C as a function of growth time t_g. We have not studied the exact mechanism leading to the resistance of Pd leaves to dewetting. It is known that dewetting initiates at grain boundaries and triple junctions.
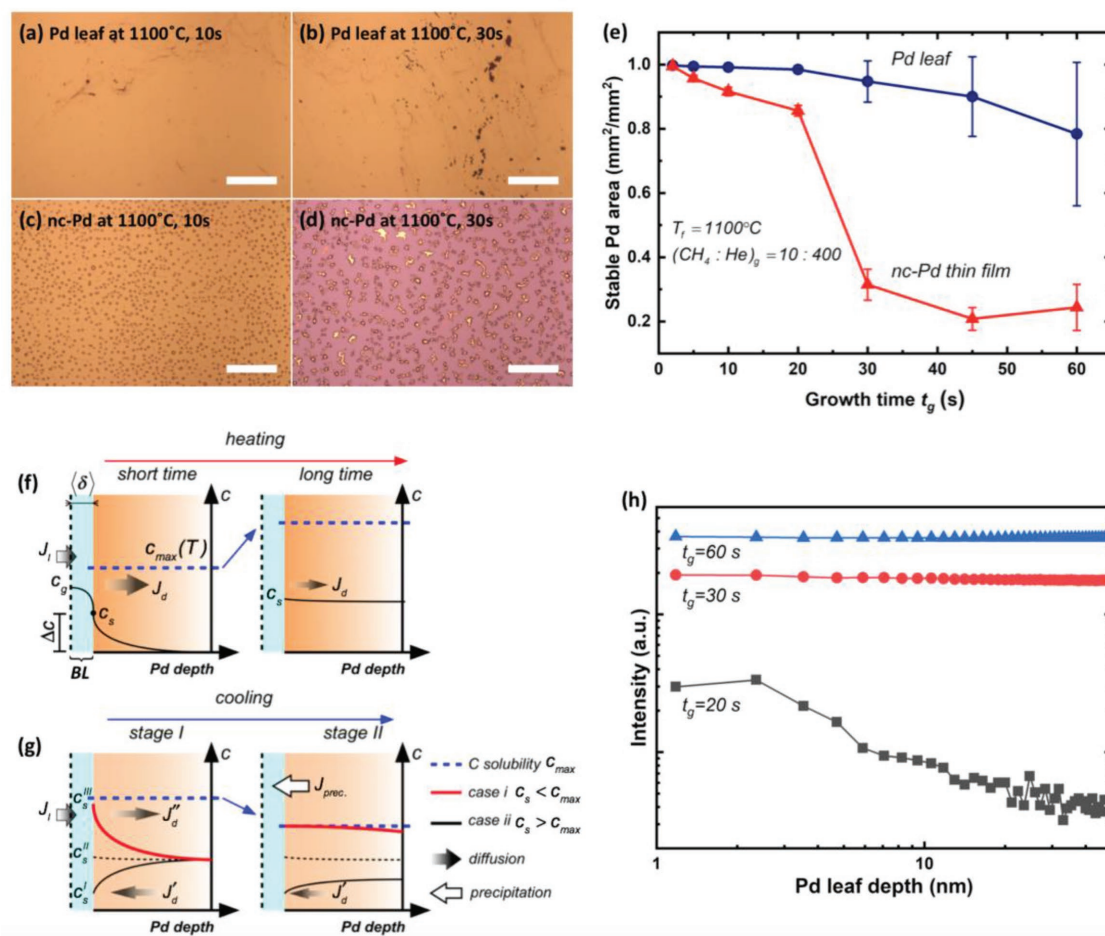

Figure 3. Synthesis kinetics on Pd leaf. a,b) Optical images of Pd leaf after annealing in a 1100 °C furnace for 10 and 30 s. c,d) Optical images of the sputtered Pd film (150 nm) after annealing in a 1100 °C furnace for 10 and 30 s, showing the surface instability of nc-Pd film at high temperature. (a)−(d) Scale bar: 50 µm. e) Instability of thin Pd films, including Pd leaf and sputtered Pd film at T_f = 1100 °C. f,g) Schematics of graphene formation kinetics showing the relationship between the carbon diffusion/segregation and carbon solubility in Pd leaf during heating and cooling. J_d is diffusion flux inward Pd when catalyst is inserted in furnace, J_d' is diffusion flux toward Pd surface, J_d'' is diffusion flux inward Pd during cooling. h) SIMS depth profiles show that the carbon concentration in Pd leaf becomes uniform as t_g increases.

**ADVANCED
SCIENCE NEWS**

www.advancedsciencenews.com

**ADVANCED
FUNCTIONAL
MATERIALS**

www.afm-journal.de

It is not surprising that the Pd leaves, which have very low triple junctions density are more resistant to dewetting. In contrast, the average grain size of 150 nm thick nc-Pd sputtered on SiO$_2$/Si substrate is ≈20 nm. This enhanced resistance enables the synthesis of high-quality graphene at high temperature, extending the growth duration to ≈45 s for Pd leaves instead of <10 s for nc-Pd.

Before presenting the graphene synthesis results, it is valuable to discuss the highly dynamic carbon kinetics required for synthesis on thin catalysts. Pd is an especially suitable metal catalyst for graphene synthesis on ultrathin films. It belongs to the second catalyst group: compared with copper, it more effectively catalyzes the dissociation of hydrocarbon and its carbon solubility is 150-fold higher at 1000 °C.[22] At synthesis temperatures, hydrocarbons like CH$_4$ quickly decompose into CH$_x$ (x = 0,1,2,3) causing a high concentration of C adatoms and addimers on the Pd surface. Carbon radicals readily dissolve into the Pd due to their lower chemical potential in bulk Pd than that on the surface as shown by molecular simulations.[23] The synthesis mechanism is the segregation of C atoms as opposed to isothermal adsorption in the case of copper catalyst.[12,14,24,25] This mechanism affords the synthesis of high-quality monolayer graphene on nanoscale thin films by a highly dynamic recipe within a growth time t_g of less than a minute. During this short t_g, carbon atoms dissolve into the Pd leaves. Whereas in the cooling stage, segregation of carbon atoms to the Pd surface and their crystallization into graphene take place.[24] Figure 3f,g depicts these two highly dynamic processes. When the Pd leaf is inserted into the furnace filled with a steady gas flow of CH$_4$ and He, a boundary layer with average thickness of $\langle\delta\rangle$ forms on the Pd surface. Importantly, since the growth time is less than a minute, the temperature variance of the catalyst with time after insertion into the hot zone has to be taken into consideration. Figure S4 (Supporting Information) displays the estimated Pd temperature T_s in the furnace for various growth times. We focus on the fast kinetics of the carbon atoms. CH$_4$ first diffuses rapidly through the boundary layer with a flux of J_I and reaches the Pd surface, decomposes into active carbon adatoms and addimers, which then invade the Pd subsurface and interior by diffusion.[23] Since Pd catalyst has high CH$_4$ decomposition reactivity,[26] concentration of the active carbon species on Pd surface c_s is determined by the concentration of CH$_4$ in gas flow c_g.

The synthesis kinetics is explained in light of Fick's diffusion laws to offer insights on the effect of synthesis duration on the carbon distribution within the catalyst for extremely short growth. As shown in Figure 3f, after a short time in the high temperature environment, carbon concentration gradient Δc between c_s and that in Pd leaf $c(\gamma, t)$ drives the diffusion flux J_d through the Pd leaf thickness. Fick's second law is used in the analysis of the carbon kinetics

$$\frac{\partial c}{\partial t} = D_{Pd}\frac{\partial^2 c}{\partial \gamma^2} \tag{1}$$

The diffusion coefficient is $D_{Pd}(T) = D_0\exp(-E_0/RT)$, where D_0 is a diffusion prefactor ≈10$^{-4.7}$ m^2 s^{-1}, E_0 is the activation energy 132 kJ mol^{-1}, and R is the gas constant 8.314 J mol^{-1}.[25] We give an approximate solution of Equation (1) in the

Supporting Information. Assuming constant c_g, carbon distribution $c(\gamma, t)$ eventually becomes homogeneous throughout the thickness after longer growth time t_g, until reaching an equilibrium state, as sketched in Figure 3f. The diffusion process is also affected by the carbon concentration with respect to the solubility limit in Pd. The solubility limit is defined as the maximum carbon concentration, $c_{max} = S_0\exp(-H_0/RT)$, where $S_0 = e^{3.2}$ and $H_0 ≈ 82.4$ kJ mol^{-1},[25] and it is varying during the growth time as the Pd temperature is also increasing within the first seconds. The solid black and the dashed blue curves in Figure 3f, respectively, illustrate the distributions $c(\gamma, t)$ for $c_s < c_{max}$ and $c_s > c_{max}$. The simple analysis demonstrates that longer growth time t_g (approaching a minute) results in uniform carbon distribution through Pd thickness (i.e., decreasing Δc). To validate these calculations by experiments, carbon concentration in Pd for t_g = 5, 10, 20, 30, 45, and 60 s are compared by secondary ion mass spectroscopy (SIMS, PEI Trift-III TOF). Figure 3h displays the representative SIMS depth profiles. Indeed, the measurements show that $t_g ≥ 30$ s gives almost uniform carbon distribution throughout Pd leaf.

The dynamics of the cooling step is crucial for graphene synthesis and layer control on catalysts of the second group by controlling carbon segregation and precipitation.[24,27,28] Dissolved carbon atoms diffuse to the surface via nonequilibrium carbon segregation as soon as temperature starts decreasing.[27] The amount of active carbon species on the Pd leaf surface at the onset of cooling significantly affects the graphene formation. Previous research has emphasized the fast and medium catalyst cooling rate (≈10 °C s^{-1} for bulk nickel[27]) regulates the amount of carbon segregation to the surface and facilitates the synthesis of a controlled number of layers. Similarly, we find that the cooling rate and surface concentration gradient Δc can be carefully balanced to achieve monolayer growth on Pd leaves.

Figure 3g illustrates the different segregation scenarios for carbon atoms in the Pd leaf during the cooling steps. Importantly, the segregation flux from the Pd is regulated by the hydrocarbon concentration in the gas boundary layer. The flux of CH$_4$ through the boundary layer (J_I) and the rate at which the active carbon species diffuse into Pd (J_d) are equal, and can be given by[29]

$$J_I = D_g\frac{c_g - c_s}{\langle\delta\rangle} \tag{2}$$

where D_g is the diffusion coefficient in gas phase, and is usually much higher than D_{Pd} in LPCVD. At the onset of cooling (cooling stage I), the carbon solubility (c_{max}) drops exponentially with temperature. But as long as $c_{max} > c_s$ and in the absence of CH$_4$ supply during cooling (i.e., $c_g = 0$), J_I drops and becomes negative, resulting in an outward carbon diffusion J'_d from the Pd to the surface, as illustrated by the black curve in Figure 3g in stage I. On the other hand, if the CH$_4$ flow is maintained during cooling $c_s \sim c_g$, $J_I \to 0$, limiting the diffusion across the Pd surface, as shown as the black dashed line in Figure 3g. Finally, if a higher concentration of CH$_4$ is introduced during cooling, that is, $c_g > c_s$, the concentration gradient in Pd will be increased as illustrated by the red line in Figure 3g, which results in more carbon diffusion J''_d into the

Pd during cooling. Eventually, at later cooling stages (stage II), $c_{max} \leq c_s$, the inward flux J_d'' will cease since the surface of Pd is saturated with carbon. During stage II, the carbon atoms start to precipitate with a flux of $J_{prec.}$, forming graphene as shown in Figure 3g in stage II. In light of this kinetics, it can be seen that a highly dynamic and fast recipe can be obtained by tight control of the hydrocarbon flow during the heating and cooling stages when the transient temperature of the sample is known in these stages.

Numerical heat and mass transport simulations are used to guide the development of new recipes based on the mechanistic understanding of graphene synthesis on Pd. Specifically, COMSOL[30] is used to simulate the transient temperature of the Pd as it is inserted and removed from the hot zone. It is important to note that the Pd temperature stabilization is governed by the thermal mass of the transfer arm, which is used to insert it into and out of the furnace. The Pd is supported on the arm throughout the synthesis process. At the end of the growth stage, the arm transports the Pd out of the furnace. The numerical simulations take these details into account (see Figure S4a, Supporting Information), which helps determine the transient temperature of the catalyst. The temperature data can in turn be used to calculate the transient carbon diffusion kinetics. The carbon concentration in the gas phase, c_g can be controlled by $(CH_4: He)_g$ (g: growth). First, we analyze the heating stage, referred to as the growth time t_g. **Figure 4**a displays the calculated carbon concentration $c(\gamma, t)$ (at%) using COMSOL for a Pd leaf at 1100 °C with the gas mixtures: $(CH_4: He)_g = 10: 400, 20: 400,$ and $50: 400$ sccm. The numerical simulations use the transient temperature and c_g to determine the carbon concentration level in the Pd leaf during this transient state. Further, the simulations show that $c_s < c_{max}$ for all of the hydrocarbon concentrations used, indicating that the duration of these short recipes (<1 min) does not allow the saturation of the catalyst with carbon. The numerical simulations also confirm that, since the diffusion in gas boundary layer is much faster than that in Pd, it is reasonable to assume $c_s \sim c_g$ on Pd surface even during the transient heating stage. These results are further validated by an approximate analytical solution for Equation (1) for Pd thin film (see the Supporting Information) as shown in Figure 4a. As expected, the analytical and numerical results vary at the onset of heating due to the neglect of diffusion through the gas boundary layer, but asymptotically converge after longer heating duration.

Next, we study the cooling stage using numerical simulations to estimate the temperature and diffusion kinetics governing the graphene formation. We validate these results by direct comparison to synthesis experiments. We simulate the retraction of the Pd leaf out of the hot zone after a certain growth time (here, $t_g = 30$ s). The numerical simulations indicate the presence of three main scenarios of carbon diffusion kinetics depending on the hydrocarbon concentration c_g during cooling. Scenario I: the hydrocarbon gas is shut down during cooling $(CH_4: He)_c = 0: 400$ sccm (c: cooling). In this case, shown in Figure 4b, c_g and c_s drop quickly and an outward flux J_d' drives the diffusion of carbon on the surface. The large amounts of segregated carbon reach the critical concentration for graphene nucleation and growth.[18,31] We experimentally validate this scenario, and the results are depicted in Figure S6 (Supporting

Information). SEM images in Figure S6a,b (Supporting Information) confirm that a large number of discrete graphite flakes are obtained in this scenario. Fuzzy edges and notably, dark regions of agglomerated carbon along Pd grain boundaries characterize the graphene coverage in Scenario I. Scenario II: the hydrocarbon concentration is maintained at a constant value during the growth and cooling stages $(CH_4: He)_c = 10: 400$ sccm as shown in Figure 4b. Under these conditions, $c(\gamma, t)$ remains approximately constant during cooling due to the absence of concentration gradient. The onset of graphene nucleation is delayed with respect to the onset of cooling in the absence of diffusion J_d'. An "incubation" period of low carbon concentration c_s on Pd surface is expected as the temperature drops. While graphene could nucleate during this stage, the growth rate is expected to be very slow. As the temperature drops further, the solubility c_{max} also decreases, eventually becoming less than c_s, which drives the segregation of carbon to the surface, and boosts the growth of graphene. The experimental validation of Scenario II confirms the formation of larger graphene coverage area, with sparse multilayer islands and more regular crystalline edges than in Scenario I (see Figure S6c,d, Supporting Information). The difference in graphene between (I) and (II) can be attributed to the carbon agglomeration rates driven by J_d' is much lower than that caused by $J_{prec.}$. Scenario III: the hydrocarbon concentration is increased at the onset of cooling $(CH_4: He)_c = 50: 400$ sccm, such that it is higher during cooling than during the growth step. This increase drives an additional inward carbon flux during cooling J_d''. Consequently, $c(\gamma, t)$ increases, driving the carbon concentration in the Pd to meet solubility limit earlier (see yellow intersection points in Figure 4b). This shortens the incubation period of the carbon atoms on the surface and initiates graphene nucleation at a higher temperature during cooling. Owing to the higher nucleation temperature compared to Scenario II, the graphene grows at a higher rate with straighter edges, indicating higher crystallinity.[32] This interesting result indicates that in catalysts of the second group, the onset of growth during cooling is precisely controlled by the hydrocarbon gas flow during this stage. Figure S6e,f (Supporting Information) displays large and uniform monolayer graphene grown on Pd leaf exhibiting hexagonal edges. This validates that increasing the gas concentration during cooling, especially c_g, can expedite the onset of graphene nucleation on Pd surface. Notably, if the cooling rate is varied, the same scenarios generally persist. Figure 4c depicts the calculation results for cases I–V but with slower cooling rate compared with Figure 4b (see Figure S4b, Supporting Information, for two cooling curves). Slow cooling delays the saturation of the Pd with carbon, as demonstrated by the delayed intersections between $c(\gamma, t)$ and c_{max} curves. This indicates that slow cooling leads to longer carbon incubation time and lower graphene nucleation temperature. Figure S6g (Supporting Information) shows SEM of the graphene obtained in case III with slow cooling rate, illustrating small flakes with irregular and fuzzy edges with the onset condition out of the optimal range due to slow cooling.

Based on these results, it is expected that high carbon precipitation flux $J_{prec.}$ at high temperatures is the key to obtain crystalline graphene monolayer with good coverage. In case IV we use $(CH_4: He)_g = 50: 400$ sccm and $(CH_4: He)_c = 50:$
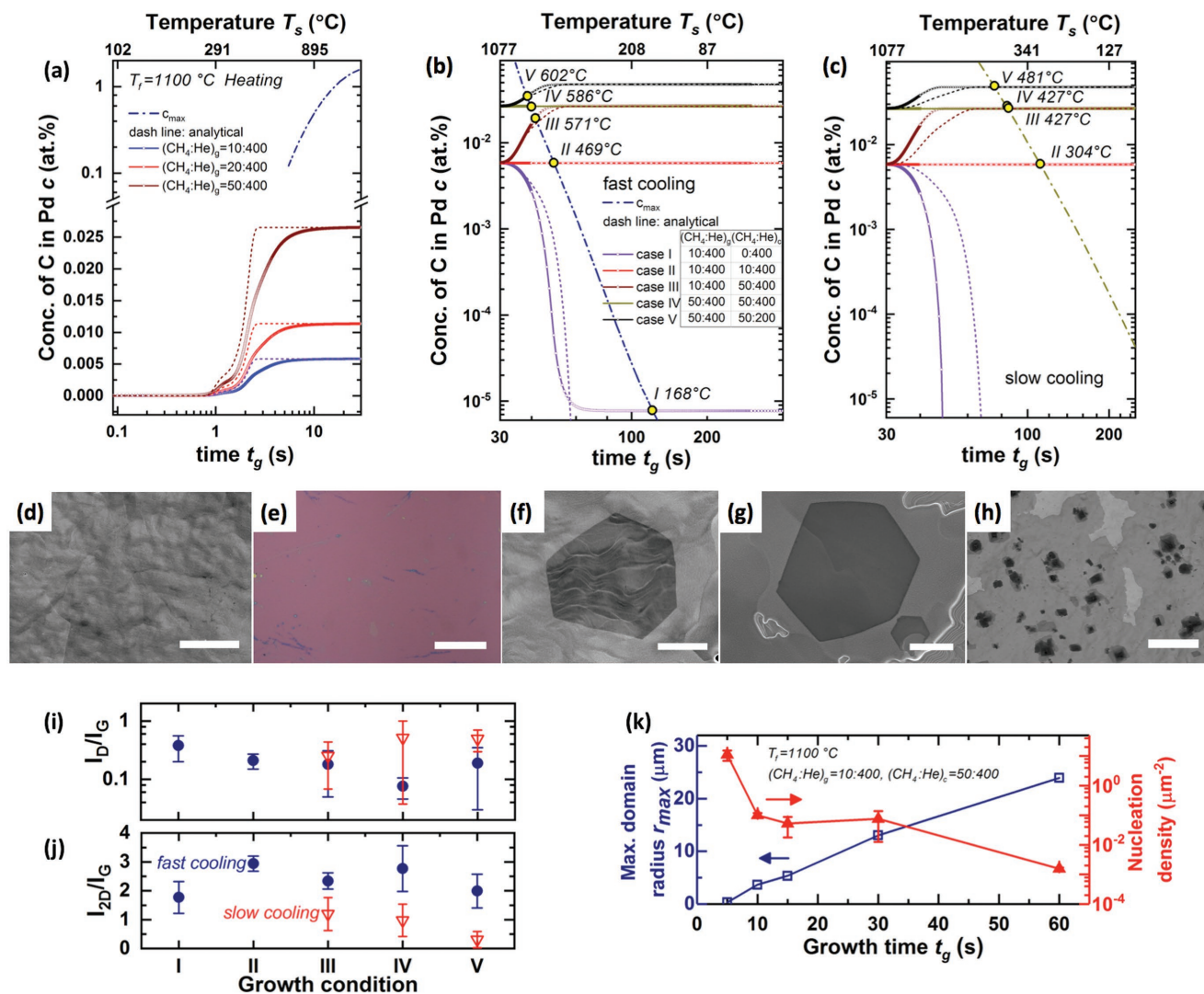
Figure 4. Carbon concentration variation in CVD process and experimental results. Simulation results from COMSOL: a) Carbon concentration (at%) in Pd leaf, which increases with growing time t_g during heating. Concentration at the steady state increases with a higher $(CH_4: He)_g$ ratio. The dashed lines are analytical solution of Equation (1) for Pd leaf. b) Carbon concentration in Pd leaf during cooling with fast cooling rate and various c_g (case I–V). All cases follow the 30 s heating at 1100 °C. c) Carbon concentration in Pd leaf during cooling with slow cooling rate. The dashed lines in (b) and (c) are analytical results. d) Scanning electron microscope (SEM) image of the as-grown graphene on Pd leaf with growth condition III, scale bar: 15 μm. e) Optical image of a transferred monolayer graphene (case IV) on SiO_2/Si substrate, scale bar: 50 μm. f) SEM image of Pd-Gr leaf with condition IV, scale bar: 10 μm. g) SEM image of Pd-Gr leaf with gas condition IV and $t_g = 60$ s, scale bar: 10 μm. h) SEM image showing the multilayer graphene with high nucleation density with cooling condition V, scale bar: 25 μm. i) Raman intensity ratio of I_{2D}/I_G for different growing conditions. j) Raman intensity ratio of I_D/I_G. k) Dependence of the maximum graphene domain radius $\left(\sqrt{A_{Gr}/\pi}\right)$ and nucleation density on growing time.

400 sccm during heating and growth, respectively. Figure 4b,c shows that carbon segregation starts at higher temperatures compared to scenarios I–III. SEM images show that using the conditions of case IV, large and hexagonal-like graphene domains can be produced and eventually merge into a monolayer of graphene, shown in Figure 2d. SEM and optical images in Figure 4d,e illustrate that large-scale uniform monolayer coverage can be achieved in cases III and IV. A single hexagonal domain in case IV, as displayed in Figure 4f, verifies the high graphene crystallinity. Notably, such graphene domain grows as t_g increases, as shown in Figure 4g and will be discussed next.

We further present the results from case V, where the synthesis condition is similar to Scenario III, but with an increase in the total hydrocarbon concentration during both growth and cooling stages. In case V, $(CH_4: He)_g = 50:400$ sccm and $(CH_4: He)_c = 50: 200$ sccm (these values are chosen in the numerical simulations to represent the maximum flow rate attainable with the CH_4 mass flow controller, which is 50 sccm). Numerical simulations in Figure 4b,c show that overall higher hydrocarbon flow further expedite the onset of nucleation, which we expect to lead to even higher $J_{prec.}$ and better crystallinity. Indeed, the synthesis results from this recipe show the large graphene coverage. However, the recipe

**ADVANCED
SCIENCE NEWS**
www.advancedsciencenews.com

**ADVANCED
FUNCTIONAL
MATERIALS**
www.afm-journal.de

led to the nucleation of multilayered graphene domains underneath the monolayer hexagons as can be seen in Figure 4f. The presence and size of these multilayer nucleation sites within the graphene domains is significantly more apparent in case V than other cases. This is attributed to the large flux of carbon atoms precipitating out of the Pd leaf when it reaches the solubility limit at a very high temperature. This indicates the existence of an "optimal" recipe where the domains are large and have a single-layer thickness, and merge to cover the whole surface with minimal coverage of multilayer regions. Results from case IV, which we consider the best recipe in this study, are shown in Figures 2d and 4e,f and Figure S6h (Supporting Information).

We use Raman spectroscopy to characterize the quality of graphene synthesized using the growth conditions: cases I–V. We find that graphene monolayers have a weak Raman signal, with no apparent D-peaks, when supported on the Pd leaf. This is not surprising in light of the known strong binding between graphene monolayers and Pd.[33] Accordingly, we transfer the graphene monolayers after synthesis via the electrochemical gas "bubbling" method[34] to clean SiO$_2$/Si substrates as presented in Figure 4e. Figure 4i,j displays the Raman intensity ratios of I_D/I_G and I_{2D}/I_G collected from a 23 µm × 23 µm region on each of the transferred graphene monolayers corresponding to cases I–V. We observe a systematic enhancement of quality, represented by the significant decrease in average I_D/I_G, from cases I to IV, that is, as the hydrocarbon flow rate is increased during cooling. Case IV shows a low I_D/I_G value of 0.08, which demonstrates exceptional quality graphene given that this is an area averaged Raman spectrum taken after transfer and mechanical manipulation. The average I_{2D}/I_G for all cases is ≈3, indicating monolayer graphene. Case V on the other hand, consistently results in lower quality and thicker graphene characterized by an increase of I_D/I_G and decrease of I_{2D}/I_G. These results are consistent with the reported studies.[35]

The quality of graphene can also be evaluated based on the size of the single-crystal domains, which is related to the nucleation density. Here, we use growth case III to illustrate the trends of the maximum domain size (defined as $\sqrt{A_{Gr}/\pi}$, A_{Gr} is domain area) and graphene nucleation density with growth time. As shown in Figure 4k, the size of the graphene domains on ultrathin Pd leaf linearly increases with t_g and the growth rate for condition III is ≈25 µm min^{-1}, which is among the highest in the literature and twice the growth rate (≈10–15 µm min^{-1}) of graphene on copper foil.[36] We explain this result by considering the even distribution of carbon throughout the Pd with longer growth time as discussed in Figure 3h. This also effectively reduces the nucleation density as shown in Figure 4k. Figure S6i–l (Supporting Information) displays the corresponding SEM images showing the evolution of monolayer graphene formation on Pd leaf.

3. Mechanical Behavior of the Pd-Gr Leaf

After synthesis, the leaves offer significant advantages for gilding owing to the strong Pd-Gr interaction, and the enhancement of the surface stiffness of the leaf. We study the shift in Raman spectra during the stretching of the as-grown monolayer

graphene on the Pd leaves. The Raman peak shifts while the leaf is stretched indicates the load transfer, and the shift rate per unit strain is proportional to the quality of graphene. After synthesis, freestanding Pd-Gr leaves can float on water surface and are transferred and glued onto the surface of a poly(methyl methacrylate) (PMMA) bar. The PMMA bar with Pd-Gr leaf is subjected to three-point bending, while Raman spectra are recorded in situ, as sketched in **Figure 5**a. This technique is widely used for testing graphene under mechanical loads by measuring the strain shift rate of the 2D and G peak.[37] Importantly, it is mentioned earlier in this article that the Raman signal from monolayer graphene on the Pd leaf is weak. Specifically, CVD synthesized graphene strongly interacts with metal catalysts of the second group changing the G and 2D wavenumbers.[33] Hybridization of the π orbitals of graphene and the d electrons of metals like Pd, Ni, and Ru modifies the Dirac cone, therefore suppresses the Raman scattering.[16,33] In this study, we use 532 nm laser with exposure time of 30 s to collect the signal of graphene on Pd. We observe blue shift of ≈37.8 cm^{-1} in frequency of the G peak and ≈33.1 cm^{-1} for the 2D peak, see Figure S7 (Supporting Information). These are similar to the variations observed in the Raman spectra of graphene on Ti and Ni.[38]

We mainly consider the G peak as representative of the deformation of the as-grown Pd-Gr leaf. When the Pd-Gr leaf deforms, clear redshift and splitting of the G peak are observed, as displayed in Figure 5b. This provides solid evidence that the strain has been transferred to the graphene and it is of uniaxial nature. Figure 5c shows the evolution of the G peak under tensile strain. The G peak is split into two subpeaks with the shift rates of ≈31.84 and ≈14.00 cm^{-1} %$^{-1}$ for ω^- and ω^+, respectively. Notably, the shifts of the G peak in our CVD-grown graphene on Pd leaf are similar to those observed in the exfoliated graphene monolayers, and the corresponding Grüneisen parameter $\gamma(G) \approx 2.27$ (see Equation (S6), Supporting Information), also matches the upper values estimated in literature.[39] Overall, the observed G peak shifts verify the exceptional quality of graphene synthesized on the Pd leaf, as it is on the same order as exfoliated graphene crystals. The large shift of the G peak is not surprising, since the adhesion of graphene on Pd is strong and thus the stress transfer is expected to be more efficient than that in graphene on polymer and copper.

Finally, we use nanoindentation of the Pd-Gr to evaluate the enhancement in surface modulus due to the addition of a monolayer graphene on the leaves. The elastic response of the Pd-Gr composite leaf is measured by indenting with a diamond-coated probe (see Figure S8, Supporting Information) via AFM (Asylum Cypher). Figure 5d shows the typical force curves of the as-received Pd leaf, and on the Pd-Gr leaf. In the current study, we present results using small loads ≈150 nN, ensuring elastic deformation at indentation depth of less than 1 nm. The as-received Pd leaf shows negligible hysteresis between loading and unloading curves, while the Pd-Gr composite shows limited hysteresis possibly due to Pd-Gr interfacial slip. For sub-nm indentation, a continuum mechanics model based on Hertz contact theory[40] can be utilized to extract the effective modulus from the unloading data: $F = \frac{4}{3} E_r \sqrt{R} \delta^{3/2}$, where F is the indentation load, δ is the displacement, $E_r = \left(\frac{1-\nu^2}{E} + \frac{1-\nu_t^2}{E_t} \right)^{-1}$,
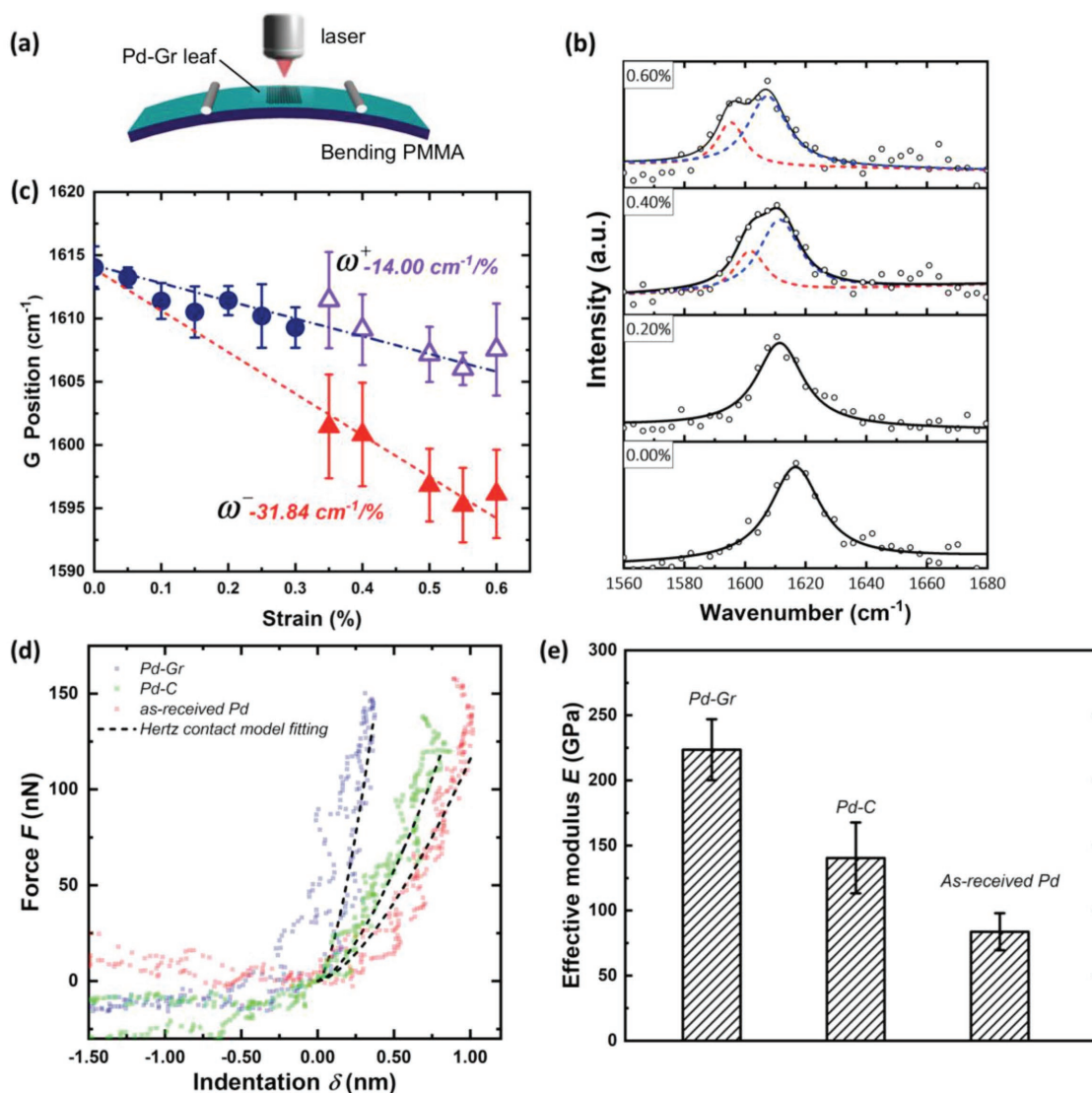
Figure 5. Mechanical behavior of the as-grown Pd-Gr leaves. a) Schematic of the in situ Raman-bending test setup. The as-grown Pd-Gr leaf is mounted on a PMMA bar, which is subjected to three-point bending. b) The evolution of Raman spectra of Pd-Gr leaf when strained during three-point bending. Redshift in G peak and splitting into two subpeaks indicate the uniaxial tension in graphene layer. c) The shift of G peak under tension for various level of strain. d) Typical force curves of the as-received Pd leaf, annealed Pd-C leaf, and the as-grown Pd-Gr leaf from AFM nanoindentation. e) The effective moduli E measured from AFM nanoindentation, showing the significant reinforcement with a CVD-grown monolayer Gr on Pd leaf.

with $E_t \approx 1050\,GPa$, $\nu_t \approx 0.2$ being the Young's modulus and the Poisson's ratio of the diamond tip. The effective modulus of Pd-Gr leaf is $223.6 \pm 23.4\,GPa$, which is close to two and a half-folds increase over the as-received leaf. This is an impressive strengthening effect considering that it is due to only a single monolayer added on the surface of an already stiff material (the Young's modulus of Pd is 121 GPa). We also report the effective modulus of areas on the same leaf, which underwent the synthesis but have not been covered with graphene, referred to as Pd-C. The Pd-Gr is higher than the Pd-C (no graphene coverage) by 60%. The origin of these enhancements can be attributed to superb mechanical behavior of the as-grown graphene layer and the defect-scarce Pd-Gr interfacial bonding. Precise mathematical modeling of this mechanical enhancement could shed new light on the route to design graphene-coated

interfaces for a variety of applications such as catalysts, coatings, and electrical connectors.

4. Conclusion

In summary, rapid LPCVD synthesis of high-quality and uniform monolayer graphene is achieved, for the first time, on the ultrathin Pd leaf providing a freestanding and cost-effective graphene-metal thin film nanocomposite. Pd leaves exhibit several qualities that made them suitable for high-quality graphene synthesis at elevated temperatures despite their thinness. To develop recipes shorter than 1 min, we use kinetics models to consider the carbon diffusion driven by concentration gradient dynamic temperature variations. The

understanding and experiments developed herein pave the route for the rational design of ultrathin graphene-metal nanocomposites. The as-grown uniform graphene layer is shown to be highly crystalline, of high quality and predominantly monolayer in thickness. In situ Raman spectroscopy during Gr-Pd stretching as well as AFM nanoindentation verify the high quality of as-grown graphene on Pd leaf and outstanding mechanical coupling at Pd-Gr interface. This study promotes graphene-based thin films and nanocomposites and opens new opportunities for the use of these materials coating and functionalization.

Supporting Information

Supporting Information is available from the Wiley Online Library or from the author.

Acknowledgements

Conflict of Interest

The authors declare no conflict of interest.

Keywords

[1] E. G. Thomsen, H. H. Thomsen, *J. Appl. Metalwork.* **1978**, *1*, 50.

[2] D. Schorsch, *J. Egypt. Archaeol.* **2001**, *87*, 55.

[3] Tutankhamun's 2nd anthropoid coffin, https://www.griffith.ox.ac.uk/gri/4rostut.html (accessed: June 2008).

[4] W. A. Oddy, *Endeavour* **1991**, *15*, 29.

[5] W. Bray, *Metal Plating and Patination*, Butterworth-Heinemann, Oxford **1993**, p. 182.

[6] E. Darque-Ceretti, E. Felder, M. Aucouturier, *Matéria* **2011**, *16*, 540.

[7] Carbide and Carbon Building, https://www.flickr.com/photos/80651083@N00/5064376349 (accessed: September 2010).

[8] a) A. K. Geim, K. S. Novoselov, *Nat. Mater.* **2007**, *6*, 183; b) C. Lee, X. Wei, J. W. Kysar, J. Hone, *Science* **2008**, *321*, 385; c) D. Prasai, J. C. Tuberquia, R. R. Harl, G. K. Jennings, K. I. Bolotin, *ACS Nano* **2012**, *6*, 1102; d) S. Li, Q. Li, R. W. Carpick, P. Gumbsch, X. Z. Liu, X. Ding, J. Sun, J. Li, *Nature* **2016**, *539*, 541.

[9] a) S. Stankovich, D. A. Dikin, G. H. Dommett, K. M. Kohlhaas, E. J. Zimney, E. A. Stach, R. D. Piner, S. T. Nguyen, R. S. Ruoff, *Nature* **2006**, *442*, 282; b) S. W. Chang, A. K. Nair, M. J. Buehler, *Philos. Mag. Lett.* **2013**, *93*, 196; c) Y. Kim, J. Lee, M. S. Yeom, J. W. Shin, H. Kim, Y. Cui, J. W. Kysar, J. Hone, Y. Jung, S. Jeon, S. M. Han, *Nat. Commun.* **2013**, *4*, 2114.

[10] K. Zhang, M. Poss, P.-J. Chen, S. Tawfick, *Adv. Eng. Mater.* **2017**, *19*, 1700475.

[11] a) X. Li, W. Cai, J. An, S. Kim, J. Nah, D. Yang, R. Piner, A. Velamakanni, I. Jung, E. Tutuc, S. K. Banerjee, L. Colombo, R. S. Ruoff, *Science* **2009**, *324*, 1312; b) S. Bae, H. Kim, Y. Lee, X. Xu, J. S. Park, Y. Zheng, J. Balakrishnan, T. Lei, H. R. Kim, Y. I. Song, Y. J. Kim, K. S. Kim, B. Ozyilmaz, J. H. Ahn, B. H. Hong, S. Iijima, *Nat. Nanotechnol.* **2010**, *5*, 574.

[12] X. H. An, F. Z. Liu, Y. J. Jung, S. Kar, *J. Phys. Chem. C* **2012**, *116*, 16412.

[13] L. Gao, W. Ren, H. Xu, L. Jin, Z. Wang, T. Ma, L. P. Ma, Z. Zhang, Q. Fu, L. M. Peng, X. Bao, H. M. Cheng, *Nat. Commun.* **2012**, *3*, 699.

[14] D. Ma, M. Liu, T. Gao, C. Li, J. Sun, Y. Nie, Q. Ji, Y. Zhang, X. Song, Y. Zhang, Z. Liu, *Small* **2014**, *10*, 4003.

[15] a) Z. P. Xu, M. J. Buehler, *J. Phys. Condens. Matter* **2010**, *22*, 485301; b) G. Giovannetti, P. A. Khomyakov, G. Brocks, V. M. Karpan, J. van den Brink, P. J. Kelly, *Phys. Rev. Lett.* **2008**, *101*, 026803.

[16] A. Dahal, M. Batzill, *Nanoscale* **2014**, *6*, 2548.

[17] C. V. Thompson, *Annu. Rev. Mater. Res.* **2012**, *42*, 399.

[18] R. S. Weatherup, B. Dlubak, S. Hofmann, *ACS Nano* **2012**, *6*, 9996.

[19] A. Cabrero-Vilatela, R. S. Weatherup, P. Braeuninger-Weimer, S. Caneva, S. Hofmann, *Nanoscale* **2016**, *8*, 2149.

[20] M. H. Griep, E. Sandoz-Rosado, T. M. Tumlin, E. Wetzel, *Nano Lett.* **2016**, *16*, 1657.

[21] D. Q. McNerny, B. Viswanath, D. Copic, F. R. Laye, C. Prohoda, A. C. Brieland-Shoultz, E. S. Polsen, N. T. Dee, V. S. Veerasamy, A. J. Hart, *Sci. Rep.* **2014**, *4*, 5049.

[22] C.-M. Sung, M.-F. Tai, *Int. J. Refract. Met. Hard Mater.* **1997**, *15*, 237.

[23] O. V. Yazyev, A. Pasquarello, *Phys. Rev. Lett.* **2008**, *100*, 156102.

[24] L. Baraton, Z. B. He, C. S. Lee, C. S. Cojocaru, M. Châtelet, J. L. Maurice, Y. H. Lee, D. Pribat, *Europhys. Lett.* **2011**, *96*, 46003.

[25] H. Yokoyama, H. Numakura, M. Koiwa, *Acta Mater.* **1998**, *46*, 2823.

[26] X. Wang, Q. Yuan, J. Li, F. Ding, *Nanoscale* **2017**, *9*, 11584.

[27] Q. Yu, J. Lian, S. Siripongert, H. Li, Y. P. Chen, S.-S. Pei, *Appl. Phys. Lett.* **2008**, *93*, 113103.

[28] Y. Miyata, K. Kamon, K. Ohashi, R. Kitaura, M. Yoshimura, H. Shinohara, *Appl. Phys. Lett.* **2010**, *96*, 263105.

[29] S. Bhaviripudi, X. Jia, M. S. Dresselhaus, J. Kong, *Nano Lett.* **2010**, *10*, 4128.

[30] a) COMSOL Chemical Reaction Engineering Module User's Guide, 5.2a, **2016**; b) COMSOL Heat Transfer Module User's Guide, 5.2a, **2016**.

[31] H. Kim, C. Mattevi, M. R. Calvo, J. C. Oberg, L. Artiglia, S. Agnoli, C. F. Hirjibehedin, M. Chhowalla, E. Saiz, *ACS Nano* **2012**, *6*, 3614.

[32] I. V. Vlassiouk, Y. Stehle, P. R. Pudasaini, R. R. Unocic, P. D. Rack, A. P. Baddorf, I. N. Ivanov, N. V. Lavrik, F. List, N. Gupta, K. V. Bets, B. I. Yakobson, S. N. Smirnov, *Nat. Mater.* **2018**, *17*, 318.

[33] D. Y. Usachov, V. Y. Davydov, V. S. Levitskii, V. O. Shevelev, D. Marchenko, B. V. Senkovskiy, O. Y. Vilkov, A. G. Rybkin, L. V. Yashina, E. V. Chulkov, I. Y. Sklyadneva, R. Heid, K. P. Bohnen, C. Laubschat, D. V. Vyalikh, *ACS Nano* **2017**, *11*, 6336.

[34] L. Gao, W. Ren, H. Xu, L. Jin, Z. Wang, T. Ma, L.-P. Ma, Z. Zhang, Q. Fu, L.-M. Peng, X. Bao, H.-M. Cheng, *Nat. Commun.* **2012**, *3*, 699.

[35] a) K. Xiao, H. Wu, H. Lv, X. Wu, H. Qian, *Nanoscale* **2013**, *5*, 5524; b) D. S. Choi, K. S. Kim, H. Kim, Y. Kim, T. Kim, S.-h. Rhy, C.-M. Yang, D. H. Yoon, W. S. Yang, *ACS Appl. Mater. Interfaces* **2014**, *6*, 19574.

[36] a) T. Wu, X. Zhang, Q. Yuan, J. Xue, G. Lu, Z. Liu, H. Wang, H. Wang, F. Ding, Q. Yu, X. Xie, M. Jiang, *Nat. Mater.* **2015**, *15*, 43; b) T. Wu, G. Ding, H. Shen, H. Wang, L. Sun, D. Jiang, X. Xie, M. Jiang, *Adv. Funct. Mater.* **2013**, *23*, 198.

[37] a) T. M. G. Mohiuddin, A. Lombardo, R. R. Nair, A. Bonetti, G. Savini, R. Jalil, N. Bonini, D. M. Basko, C. Galiotis, N. Marzari, K. S. Novoselov, A. K. Geim, A. C. Ferrari, *Phys. Rev. B* **2009**,

79, 205433; b) C. Androulidakis, E. N. Koukaras, J. Parthenios, G. Kalosakas, K. Papagelis, C. Galiotis, *Sci. Rep.* **2015**, *5*, 18219.

[38] H. Xu, X. Wu, X. Li, C. Luo, F. Liang, E. Orignac, J. Zhang, J. Chu, *Carbon* **2018**, *127*, 491.

[39] a) O. Frank, G. Tsoukleri, J. Parthenios, K. Papagelis, I. Riaz, R. Jalil, K. S. Novoselov, C. Galiotis, *ACS Nano* **2010**, *4*, 3131; b) S. R. Na,

X. Wang, R. D. Piner, R. Huang, C. G. Willson, K. M. Liechti, *ACS Nano* **2016**.

[40] a) W. C. Oliver, G. M. Pharr, *J. Mater. Res.* **1992**, *7*, 1564; b) Y. Gao, S. Kim, S. Zhou, H.-C. Chiu, D. Nélias, C. Berger, W. de Heer, L. Polloni, R. Sordan, A. Bongiorno, E. Riedo, *Nat. Mater.* **2015**, *14*, 714.

1804068 (11 of 11)